Multidimensional Nano-Imaging of Structure, Coupling, and Disorder in Molecular Materials

Sven A. Dönges, R. Peyton Cline, Steven E. Zeltmann, Jun Nishida, Bernd Metzger, Andrew M. Minor, Joel D. Eaves, and Markus B. Raschke*

Read Online

ACCESS | Metrics & More | Article Recommendations | Supporting Information

ABSTRACT: A hierarchy of intramolecular and intermolecular interactions controls the properties of biomedical, photophysical, and novel energy materials. However, multiscale heterogeneities often obfuscate the relationship between microscopic structure and emergent function, and they are generally difficult to access with conventional optical and electron microscopy techniques. Here, we combine vibrational exciton nanoimaging in variable-temperature near-field optical microscopy (IR *s*-SNOM) with four-dimensional scanning transmission electron microscopy (4D-STEM), and vibrational exciton modeling based on density functional theory (DFT), to link local microscopic molecular interactions to macroscopic three-dimensional order. In the application to poly(tetrafluoroethylene) (PTFE), large spatio-spectral heterogeneities with C−F vibrational energy shifts ranging from sub-cm^{-1} to $\gtrsim 25$ cm^{-1} serve as a molecular ruler of the degree of local crystallinity and disorder. Spatio-spectral-structural correlations reveal a previously invisible degree of highly variable local disorder in molecular coupling as the possible missing link between nanoscale morphology and associated electronic, photonic, and other functional properties of molecular materials.

KEYWORDS: *multimodal, vibrational exciton, nanoimaging, poly tetrafluoroethylene, density functional theory, model Hamiltonian, transmission electron microscopy*

INTRODUCTION

Increasingly complex polymers and other supramolecular systems have a wide range of applications in biomedical sensing,[1,2] flexible organic solar cells,[3,4] organic (multi)-ferroics,[5,6] organic thermoelectrics,[7,8] or novel fuel cells.[9,10] Functional properties in these systems are emergent—they originate in molecular interactions over a hierarchy of physical scales in energy and length. In condensed phases of polymers, intrachain and interchain coupling are sensitive to small variations in the kinetic and thermodynamic conditions, from the synthesis to post-processing and device fabrication.[11−13] However, direct access to structural details from molecular to micrometer scales has remained elusive for both atomistic computations and experimental spectroscopies and imaging.

Access to the complex interplay between structure and coupling thus requires a multimodal and multiscale approach to simultaneously probe molecular degrees of freedom across the range of relevant length scales.[14] Despite atomic resolution, electron imaging cannot readily probe the low energy scales of, e.g., van der Waals forces and hydrogen bonds.[15] This low-energy landscape is covered by infrared (IR) spectroscopy, where vibrational resonances act as exquisitely sensitive probes of molecular coupling, yet conventionally with limited spatial resolution.
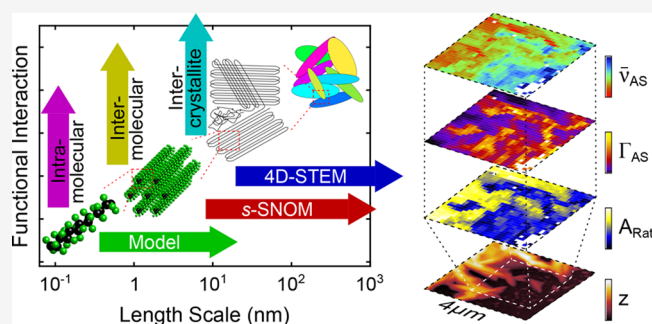
In this work, we combine infrared vibrational nano-spectroscopy and nanoimaging (*s*-SNOM) with four-dimensional transmission electron microscopy (4D-STEM), informed by density functional theory (DFT)-based vibrational exciton modeling, to probe how molecular level interactions relate to nanoscale morphology at the example of poly-(tetrafluoroethylene) (PTFE) (see Figure 1A). Correlated to the local nanocrystal orientation provided by 4D-STEM, we resolve nanometer spatial variations in vibrational frequencies from sub-cm^{-1} to $\gtrsim 25$ cm^{-1}, which we attribute to the exceptional sensitivity of vibrational excitons to the local environment. Thus, these vibrational excitons serve as a *molecular ruler* probing the degree of local order and crystallinity and allow to distinguish surface, bulk, and nanostructural heterogeneity. This multimodal experimental and theoretical approach is readily extendable to a broad range
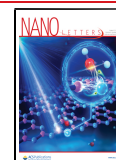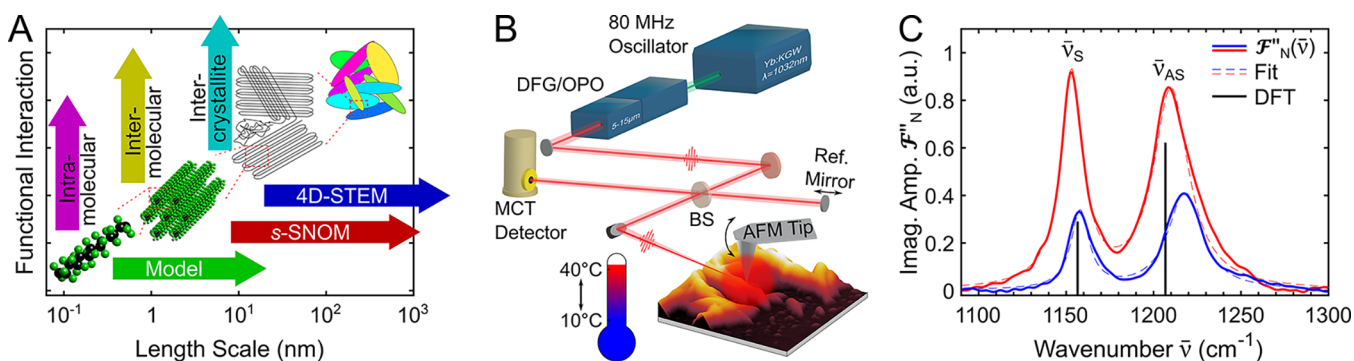
Figure 1. (A) Representation of coupled domain formation and relevant length scales determining the nano- and microscale properties of polymers, with techniques to access the relevant elementary interactions. (B) Nano-FTIR experimental setup (MCT, mercury cadmium telluride; BS, beam splitter; DFG, difference frequency generation; OPO, optical parametric oscillator). (C) Representative nano-FTIR spectra on high (red) and low (blue) topographic regions on melted poly tetrafluoroethylene (PTFE). Vibrational modes (vertical lines) of symmetric ($\overline{\nu}_S$) and antisymmetric ($\overline{\nu}_{AS}$) stretch modes based on density functional theory (DFT) for an isolated, infinite PTFE chain (black lines, offset to match with experiment).
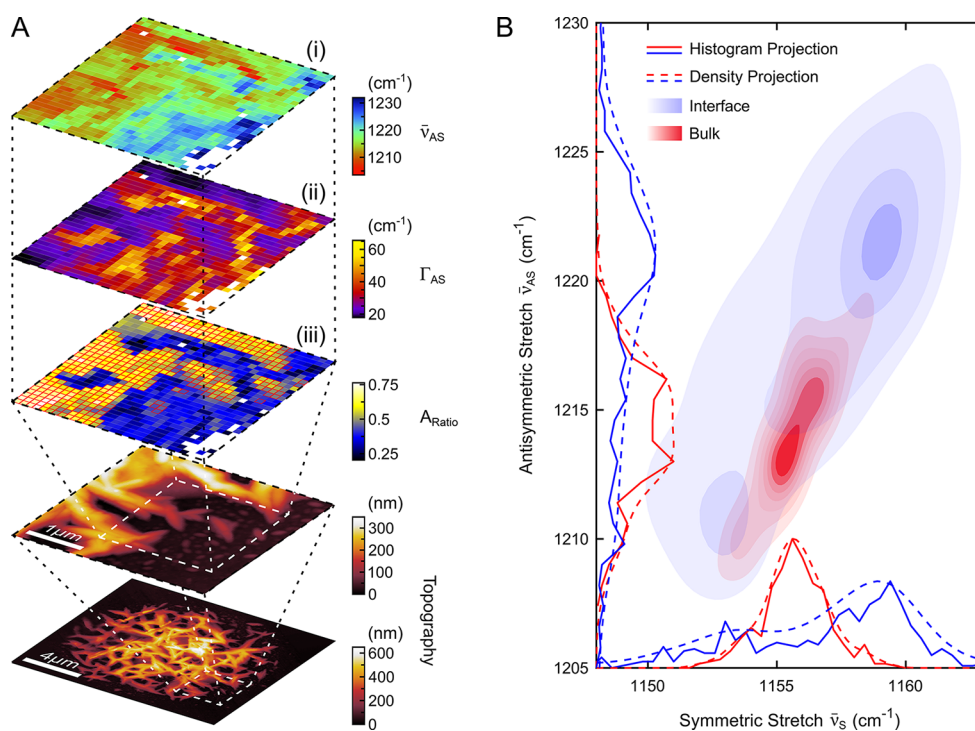

Figure 2. (A) Nano-FTIR images at the edge of a PTFE bead of (i) antisymmetric stretch mode peak position ($\overline{\nu}_{AS}$), (ii) line width (Γ_{AS}), and (iii) ratio between symmetric and antisymmetric peak areas (A_{Ratio}). (B) Corresponding density-correlation plot between $\overline{\nu}_S$ and $\overline{\nu}_{AS}$. The subset of data points of the red subensemble in Panel (B) is indicated by red squares in Panel (A (iii)) and selected based on a strong spectral phase response with $\Phi = \arctan(\mathscr{F}''_N/\mathscr{F}'_N) > 80°$.

of photophysical, electric, biological, or catalytic molecular materials.

EXPERIMENT

We investigate PTFE as a simple fluorinated polymer with many commercial and technological applications.[16] In addition, PTFE serves as a model system for advanced fluorinated polymer applications such as Nafion-based fuel cells, fluorinated ethylene propylene (FEP) insulators, and the chemically inert perfluoroalkoxy alkane (PFA).[9,16] Like PTFE, the high thermal stability, chemical inertness, and low coefficients of friction of these compounds are due to the

strength of the C−F bond and the high electronegativity and low polarizability of fluorine.[17]

PTFE samples were prepared by melting sparsely distributed micrometer-sized semicrystalline PTFE beads (Sigma−Aldrich, Product No. 430935-5G) on a template stripped gold substrate at 385 °C for 30 min. Subsequent slow cooling at 1−2 °C/min results in a high degree of crystallinity, as previously established.[18,19] with isolated PTFE aggregates forming elongated structures extending in size from few to several hundred nanometers[19,20] (see Figure S4A in the Supporting Information).

PTFE exhibits complex structural phases within a narrow temperature and pressure range near ambient conditions.[21] A structural phase transition at 19 °C is associated with a slight
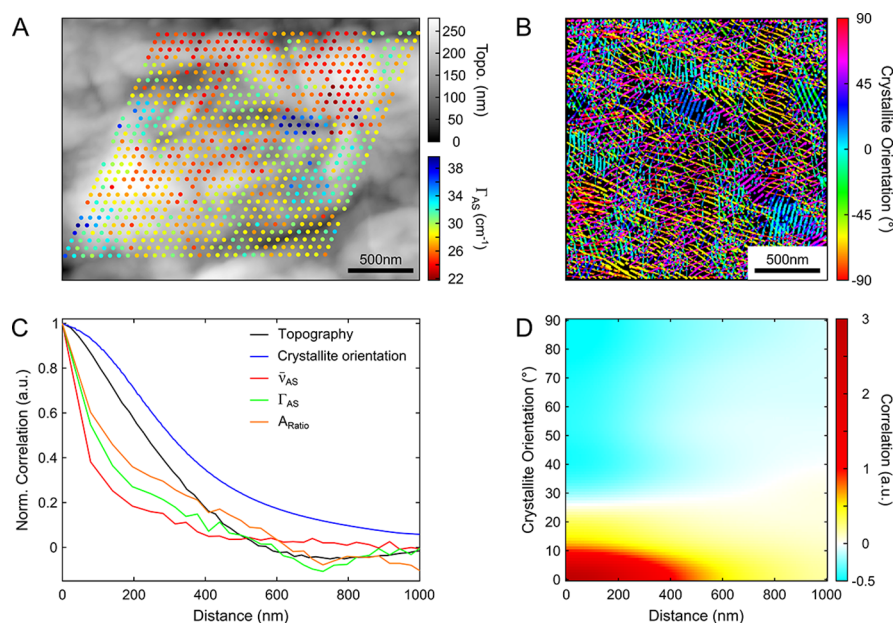
Figure 3. (A) Nanoscale variation of Γ_{AS} on microtomed PTFE measured by nano-FTIR spectroscopy. (B) Flowline chart of 4D-STEM measurement of the nanolocalized crystal orientation in the same general sample region as shown in Panel (A). (C) Corresponding radial autocorrelation of representative structural (topography, crystal orientation) and spectral parameters ($\overline{\nu}_{AS}$, Γ_{AS}, and A_{Ratio}). (D) Radial autocorrelation for different crystal angles for the data is shown in Panel (B).

untwisting of the PTFE helical conformation from a non-commensurable 13_6 configuration (form II) to a commensurable 15_7 configuration (form IV). Above 30 °C (form I), the crystallinity of PTFE decreases due to an increasing number of helix reversal defects and the coexistence of the 15_7 conformation with a planar (2_1) conformation.[21,22] Using X-ray diffraction (XRD), we confirm the samples to be highly crystalline, with interchain spacing of 5.65 Å, indicative of form IV.[23,24] Fits to the Scherrer equation reveal an average nanocrystallite size of ~40 nm (see section VI in the Supporting Information).

For the scanning transmission electron microscopy (STEM) experiments, PTFE flakes were microtomed from a solid stick of PTFE (Grainger), with thicknesses ranging from ~100 nm to ~1 μm and deposited on 10-nm SiN windows in a TEM grid (Norcada, Canada).

IR scattering scanning near-field optical microscopy (s-SNOM) nanospectroscopy and nanoimaging is performed by illuminating the metallized tip of an atomic force microscope operating in tapping mode (nanoIR2-s prototype, Anasys Instruments/Bruker) with femtosecond infrared pulses (Flint, Light Conversion; Levante OPO + HarmoniXX DFG, APE GmbH) (see Figure 1B). The broadband IR pulses are centered at ~1200 cm^{-1} with ~150 cm^{-1} spectral bandwidth (fwhm) to cover both the symmetric $\overline{\nu}_S$ and antisymmetric $\overline{\nu}_{AS}$ C−F stretch modes with spectral irradiance of ~2.5 W/cm^2/cm^{-1}. Through interferometric heterodyne detection of the tip scattered signal, demodulated at the second-harmonic of the AFM cantilever tapping frequency, we acquire complex valued nanolocalized Fourier transform infrared (nano-FTIR) spectra (Figure 1C, solid line) with 3−6 cm^{-1} resolution, as previously established.[25,26] By fitting the sum of two complex valued Lorentzians (Figure 1C, dashed line) to the real $\mathcal{F}'_N$ and imaginary $\mathcal{F}''_N$ part of the near-field spectra, we derive seven independent fitting parameters for each spectrum: amplitudes a_S, a_{AS}; line widths Γ_S, Γ_{AS}; center frequencies $\overline{\nu}_S$, $\overline{\nu}_{AS}$ for the

symmetric (S) and antisymmetric (AS) stretch modes; and a nonresonant dielectric term ϵ_∞. Because of the high spectral signal-to-noise the fitting of individual spectra is remarkably robust with estimated errors of ±2% for a_S and a_{AS}, ±1 cm^{-1} for Γ_S and Γ_{AS}, and less than ±1 cm^{-1} for $\overline{\nu}_S$ and $\overline{\nu}_{AS}$. By measuring nano-FTIR spectra on two-dimensional grids with 20 × 20 to 50 × 50 individual spectra and 50−100 nm spacing between sampling locations, we compose hyperspectral images of varying pixel density of PTFE (see section I in the Supporting Information for details).

RESULTS

Experimental Results. Figure 2A shows hyperspectral s-SNOM images at the edge of an ~10-μm-sized melted PTFE bead. In the AFM image (bottom panel), the topographically low areas correspond to the gold substrate, while elevated areas show the network of PTFE aggregates. Panels (i)−(iii) in Figure 2A show maps of $\overline{\nu}_{AS}$, Γ_{AS}, and the ratio $A_{Ratio} = A_S/A_{AS}$ of the peak areas of the symmetric A_S and antisymmetric A_{AS} modes ($A_i = a_i \times \Gamma_i$). Each pixel corresponds to a fit to one of 30 × 30 nano-FTIR spectra. Missing pixels represent spectra with an insufficient signal-to-noise ratio for identifying separable spectral features. The spatial variations in $\overline{\nu}_{AS}$, Γ_{AS}, and A_{Ratio} largely correlate with the topographic features of the sample. The data points highlighted by red squares in Panel (iii) in Figure 2A exhibit a strong spectral phase response,

$$\Phi = \arctan\left(\frac{\mathcal{F}''_N}{\mathcal{F}'_N}\right) > 80°$$

and correlate with regions of high topography. Furthermore, we observe a strong correlation between $\overline{\nu}_S$ and $\overline{\nu}_{AS}$ with large spread in center frequencies of $\Delta\overline{\nu} \approx 20-25$ cm^{-1} (Figure 2B), that exceeds the fit uncertainty of <1 cm^{-1} by more than an order of magnitude. In addition, the subensembles with a weak (blue) and strong (red) near-field response separate spectrally.
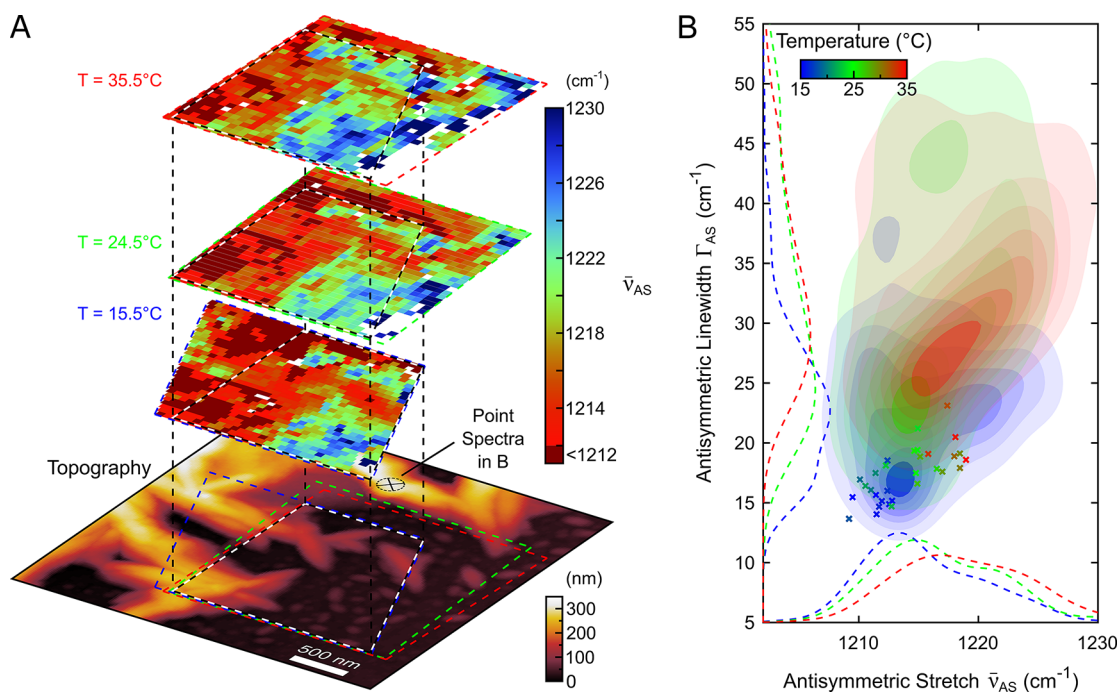
Figure 4. (A) Temperature-dependent nano-FTIR imaging of $\bar{\nu}_{AS}$ for 15.5, 24.5, and 35.5 °C, showing a spectral blue shift with increasing temperature. (B) Density correlation between $\bar{\nu}_{AS}$ and Γ_{AS} for the data sets in Panel (A) with overall blue shift correlated with spectral broadening. Projections of density distributions (dashed lines). Crosses (x) mark temperature dependent point spectra at the location marked in the topography image in Panel (A).

The solid and dashed lines represent the projection of the histogram and density distributions of the two subsets of data on the x- and y-axes, respectively.

To relate the spectral properties to the structural properties of PTFE, we perform correlative imaging of hyperspectral nano-FTIR and 4D-STEM of the microtomed PTFE samples (Figure 3). The AFM topography and the spatial variations in Γ_{AS} for an ∼2 μm × 2 μm sample area (Figure 3A) are similar to characteristics observed on melted PTFE (Figure 2A(ii)). The corresponding local orientation of PTFE crystallites with, in part, three dimensionally overlapping domains is represented in a 4D-STEM flowline chart (Figure 3B) with the corresponding radial and angular autocorrelation function[27] shown in Figure 3D. The radial correlation functions (Figure 3C) for the spectral features ($\bar{\nu}_{AS}$ (red), Γ_{AS} (green), and A_{Ratio} (orange)) show little correlation for a separation exceeding 200 nm, while the radial correlation of topography (black) and crystal orientation (blue) continues beyond 300 and 400 nm, respectively.

The radial correlation lengths, as a measure of domain size, for the s-SNOM and 4D-STEM measurements (Figure 3C) are in overall good agreement with 4D-STEM values generally higher. We attribute this small difference to the interior morphology of microtomed samples dominating the 4D-STEM results, while s-SNOM more selectively probes the near surface regions to depths of ∼20 nm.[14] Furthermore, 4D-STEM measurements inherently correlate crystal orientations of the front and back of the sample to each other, thus resulting in longer correlation lengths.[28]

To access the spectral signatures of structural changes related to the phase transitions of PTFE at 19 and 30 °C, we perform temperature-dependent hyperspectral array imaging on the melted PTFE samples (Figure 4A). A spectral blue shift $\Delta\bar{\nu}_{AS} \approx 7$ cm^{-1} and broadening $\Delta\Gamma_{AS} \approx 10$ cm^{-1} correlated

with increasing temperature are observed (Figure 4B). These changes are not caused by a change in morphology of the spectral features but reflect a general blue shift and broadening with temperature, as exemplified by the temperature-dependent point spectra shown in Figure 4B (crosses) at the location marked in Figure 4A. The spectral shift is in good agreement with theoretical predictions of the frequency shift associated with the phase transition between form II and form IV.[29]

The temperature-dependent measurements (Figure 4) confirm that structural reorganization on the polymer-chain level in the phase transition between forms II and IV affects the vibrational spectra with shifts of up to 7 cm^{-1}. The phase transition in PTFE is also highly sensitive to pressure,[22,23] suggesting that local strain and phase coexistence can contribute to the observed range of spectral frequencies. The spectral broadening with increasing temperature further points to an increased disorder, as expected for the high-temperature form I.[22,23]

Theory and Modeling. To connect the observed spectral features to underlying molecular structure and morphology, we use DFT calculations of isolated, single PTFE chains, periodic in one dimension, to parametrize a vibrational exciton Hamiltonian. Specifically, we compute the spectrum from the vibrational normal modes in both the 13_6 (form II) and 15_7 (form IV) helical conformers (see section I in the Supporting Information for details). The IR spectrum is dominated by the symmetric and antisymmetric normal modes. These two normal modes are, in turn, in-phase superpositions of the symmetric and antisymmetric C−F local mode stretches from individual monomers along the polymer backbone.

These calculations find that the two stretching modes are split by ≈50 cm^{-1}, in good agreement with the experiment (Figure 1C). Additionally, the calculated vibrational modes of the 15_7 helical configuration are blue-shifted by ∼3 cm^{-1} and

~4 cm^{-1}, with respect to the 13$_6$ helix for the symmetric and antisymmetric modes, respectively. These results are also qualitatively similar to experimental findings.

The parameters of our model Hamiltonian follow from an identification of the fundamental interactions between the local C−F oscillators within a sample of PTFE. Each C−F oscillator along the polymer backbone is a local mode with stretching frequency $\bar{\nu}$. The two local modes attached to the same carbon atom experience through-bond coupling, akin to kinetic coupling, via the matrix element J.[30] Through-space coupling occurs between oscillators on different carbon atoms through the dipole−dipole interaction V. After expanding the dipoles in terms of the local mode coordinates $\{q_1, q_2, \cdots\}$, quantizing in terms of the local mode harmonic oscillator basis and keeping only terms in the one-exciton subspace, the vibrational exciton Hamiltonian becomes[31]

$$\mathcal{H} = \bar{\nu} \sum_l a_l^\dagger a_l + \frac{J}{2} \sum_{\langle l,l' \rangle} (a_l^\dagger a_{l'} + a_{l'}^\dagger a_l)$$
$$+ \frac{\lambda}{2} \sum_{k,l \neq k} V_{kl}(a_k^\dagger a_l + a_l^\dagger a_k) \tag{1}$$

The first term is the sum over the degenerate C−F local mode oscillators, where a_l is the annihilation operator for local mode l. The second term is the through-bond coupling, where the notation $\sum_{\langle l,l' \rangle}$ restricts the sum to pairs of local modes attached to the same carbon. The third term is the through-space coupling, parametrized by λ and mediated through the transition dipole-transition dipole tensor,

$$V_{kl} = \hat{\boldsymbol{m}}_k \cdot \left(\frac{\boldsymbol{1} - 3\hat{\boldsymbol{r}}_{kl}\hat{\boldsymbol{r}}_{kl}}{r_{kl}^3} \right) \cdot \hat{\boldsymbol{m}}_l$$

where r_{kl} is the vector between the centers of the point transition dipoles $\boldsymbol{m}_k$ and $\boldsymbol{m}_l$ that are centered at $\boldsymbol{r}_k$ and $\boldsymbol{r}_l$, respectively. Hats denote unit vectors and $V_{kl} = 0$ for oscillators attached to the same carbon. Note that the expression for the dipole−dipole coupling between *transition dipoles* (V_{kl}) is the same as the dipole−dipole coupling between *static dipoles*.[32] We will exploit this fact to facilitate the interpretation for the results of this model.

From the parametrization of a single strand, we simulate a sample of multiple PTFE strands consisting of thousands of atoms—a calculation that would be intractable for a vibrational-mode analysis using only DFT. As such, we construct an idealized version of the experiment—a finite-sized hexagonal bundle (Figure 5 inset)—to represent an isolated sample of microcrystalline PTFE, with PTFE molecules parallel to each other with a uniform interchain distance of 5.7 Å. We compute the spatially resolved optical spectrum one single strand at a time, similar in spirit to how the experiments probe spatially distinct regions. We find that the vibrational frequencies of PTFE chains at the exterior of this sample are blue-shifted by $\Delta\bar{\nu}_S \approx 4$ cm^{-1} and $\Delta\bar{\nu}_{AS} \approx 7$ cm^{-1}, compared to chains in the interior (Figure 5), allowing us to identify an electrostatic origin for the experimentally observed spatio-spectral heterogeneity (see discussion below).

■ DISCUSSION

In the following, we discuss the potential origin of the observed large spatial and spectral heterogeneity in PTFE in context with earlier work on PTFE and other polymers. We attribute the anomalously large peak shifts (Figure 2) to intramolecular
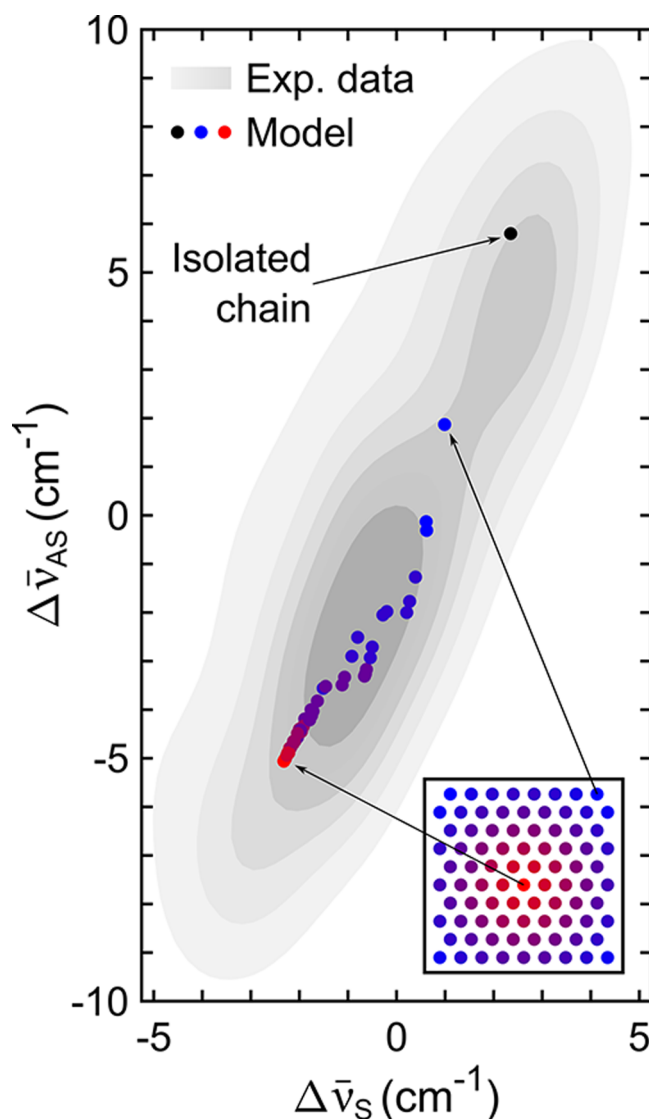

Figure 5. Variation in local mode vibrational frequency shifts, $\Delta\bar{\nu}_S \equiv \bar{\nu}_S - \langle\bar{\nu}_S\rangle$, as a function of PTFE strand location within a PTFE crystal, as determined by the vibrational exciton model, in comparison to experimental nano-FTIR data from Figure 2. The inset shows a cross section from a calculation using the vibrational exciton model for a bundle with lattice spacing matching the 15$_7$ crystal structure. The oscillators in the interior (red) of the bundle red-shift relative to those on the exterior (blue).

and intermolecular vibrational coupling among densely packed C−F vibrational oscillators with their characteristic large oscillator strength and associated transition dipole moment (estimated at ≥ 1 D/nm^3; see section II in the Supporting Information). Both vibrational frequencies $\bar{\nu}_S$ and $\bar{\nu}_{AS}$ red-shift in the bulk regions of the PTFE crystal, compared to the interfacial, or exterior, regions with the coupled oscillators in the interior surrounded by molecules that provide a polarization. The exciton model is analogous to the reaction field in the Onsager theory describing polar solvation.[32] Just as the reaction field lowers the solvation energy of polar solvation and leads to a solvation Stokes shift, the crystal polarization acts more strongly on the transition dipoles for oscillators that are in the interior of the crystal than it does for those on the surface where there are fewer molecules to polarize. The result

is a more pronounced red shift for oscillators in the interior of the crystal, compared to those on the surface (Figure 5).[32−34]

This interpretation is consistent with the observed red shift (Figure 2) for topographically higher areas that we associate with bulk PTFE, in contrast to the blue-shifted topographically thinner areas, where interfacial regions dominate the *s*-SNOM response. In these topographically thinner regions, where the PTFE crystallites have diameters on the order of 10−50 nm, the *s*-SNOM signal is dominated by the large interface to bulk ratios with significantly broader spectral features, indicating a larger heterogeneity with multiple subensembles within the probe volume of the tip.[26] In addition, in structurally disordered sample regions (like small PTFE aggregates) where individual PTFE chains do not assemble in a perfectly crystalline structure, a decrease in intramolecular and intermolecular coupling results in a reduced vibrational delocalization, causing a spectral blue shift, as observed in sample areas with smaller PTFE aggregates. Different influences of the PTFE/air and PTFE/substrate interface on the local and overall crystallinity of these aggregates could influence the *s*-SNOM results, depending on their exact dimensions and morphology. The PTFE/Au interface could impact the formation of crystalline PTFE differently from the air interface, thus influencing the thickness of the disordered interfacial region between the substrate and PTFE and the overall observed heterogeneity of especially small PTFE aggregates.

These combined results suggest that multiple mechanisms such as the coexistence of different structural phases, varying surface to volume ratios, and local disorder compound and produce the wide range of spectral variations we observe. Previously, far-field infrared spectroscopy studies have indicated heterogeneity in PTFE that has been interpreted as coexistence of amorphous and crystalline sample regions.[29,35] Structural disorder has also been observed in a wide range of X-ray and electron diffraction studies; this disorder has been associated with the form II to form IV and form I structural phase transitions[22−24,36] and correlates with the temperature-dependent spectral broadening that we observe (Figure 3). Heterogeneities on the submicrometer and molecular scale have been identified in polyethylene[37,38] and shown to alter physical properties such as melt viscosity or drawability,[39] yet without spatially resolving them. In polymer blends, composites, and gels, significant efforts with multiscale modeling[40−43] and experimental observations[44−47] have been made to predict microscale structure. Thus, with the sensitivity of vibrational excitons to crystallinity, morphology and local dielectric environment, our integrated approach can provide deeper insight into the nanoscale structure−functional relationship in these materials.

SUMMARY

Our multimodal combination of imaging and theory shows a surprisingly high level of hierarchical complexity in PTFE, despite its apparent molecular and structural simplicity. These heterogeneities are sensitively reflected in the formation of intramolecular and intermolecular vibrational excitons. Their spatial wave function delocalization, facilitated by the high density of vibrational oscillators and their large transition dipole moments, provides a quantum imaging sensor for local molecular disorder. The resulting real-space view shows how intramolecular and intermolecular interactions control polymer morphology from the nanoscale to mesoscale. The ability to spatially resolve low-energy structural and dynamic macromolecular landscapes will lead to a deeper understanding of how complex molecular systems gain their macroscopic properties and functions in polymers and polymer composites. Our multimodal approach of simultaneous access to structure and coupling down to the molecular scale is readily extendable to any molecular systems, providing the critical link to associated electronic, photonic, carrier transport, and other functional properties of molecular materials.

■ ASSOCIATED CONTENT

ⓈⒾ Supporting Information

The Supporting Information is available free of charge at https://pubs.acs.org/doi/10.1021/acs.nanolett.1c01369.

> Description of the methods, transition dipole moment estimate, extended hyperspectral heterogeneity, nanomechanical property mapping, near-field interaction between tip and sample, X-ray diffraction, vibrational delocalization, and vibrational exciton model (PDF)

■ AUTHOR INFORMATION

Corresponding Author

Markus B. Raschke − *Department of Physics, Department of Chemistry, and JILA, University of Colorado, Boulder, Colorado 80309, United States;* ⓞ orcid.org/0000-0003-2822-851X; Email: markus.raschke@colorado.edu

Authors

Sven A. Dönges − *Department of Physics, Department of Chemistry, and JILA, University of Colorado, Boulder, Colorado 80309, United States;* ⓞ orcid.org/0000-0003-1363-9519

R. Peyton Cline − *Department of Chemistry, University of Colorado, Boulder, Colorado 80309, United States;* ⓞ orcid.org/0000-0001-8293-1279

Steven E. Zeltmann − *Department of Materials Science and Engineering, University of California, Berkeley, California 94720, United States*

Jun Nishida − *Department of Physics, Department of Chemistry, and JILA, University of Colorado, Boulder, Colorado 80309, United States;* ⓞ orcid.org/0000-0001-7834-8179

Bernd Metzger − *Department of Physics, Department of Chemistry, and JILA, University of Colorado, Boulder, Colorado 80309, United States;* ⓞ orcid.org/0000-0002-9027-8676

Andrew M. Minor − *Department of Materials Science and Engineering, University of California, Berkeley, California 94720, United States; National Center for Electron Microscopy, Molecular Foundry, Lawrence Berkeley, National Laboratory, Berkeley, California 94720, United States;* ⓞ orcid.org/0000-0003-3606-8309

Joel D. Eaves − *Department of Chemistry, University of Colorado, Boulder, Colorado 80309, United States;* ⓞ orcid.org/0000-0002-9371-1703

Complete contact information is available at:
https://pubs.acs.org/10.1021/acs.nanolett.1c01369

Author Contributions

M.B.R., B.M., S.A.D., and J.N. conceived the experiment. S.A.D., B.M., and S.E.Z. prepared the samples. S.A.D. and B.M. performed the nano-FTIR measurements. S.A.D. analyzed the

■ **REFERENCES**

(1) Hammock, M. L.; Chortos, A.; Tee, B. C. K.; Tok, J. B. H.; Bao, Z. 25th anniversary article: The evolution of electronic skin (E-Skin): A brief history, design considerations, and recent progress. *Adv. Mater.* **2013**, *25*, 5997−6038.

(2) Park, S. H.; Lee, H. B.; Yeon, S. M.; Park, J.; Lee, N. K. Flexible and Stretchable Piezoelectric Sensor with Thickness-Tunable Configuration of Electrospun Nanofiber Mat and Elastomeric Substrates. *ACS Appl. Mater. Interfaces* **2016**, *8*, 24773−24781.

(3) Meng, L.; Zhang, Y.; Wan, X.; Li, C.; Zhang, X.; Wang, Y.; Ke, X.; Xiao, Z.; Ding, L.; Xia, R.; Yip, H. L.; Cao, Y.; Chen, Y. Organic and solution-processed tandem solar cells with 17.3% efficiency. *Science* **2018**, *361*, 1094−1098.

(4) Polman, A.; Knight, M.; Garnett, E. C.; Ehrler, B.; Sinke, W. C. Photovoltaic materials: Present efficiencies and future challenges. *Science* **2016**, *352*, aad4424.

(5) Horiuchi, S.; Tokura, Y. Organic ferroelectrics. *Nat. Mater.* **2008**, *7*, 357−366.

(6) Jin, J.; Lu, S.-G.; Chanthad, C.; Zhang, Q.; Haque, M. A.; Wang, Q. Multiferroic Polymer Composites with Greatly Enhanced Magnetoelectric Effect under a Low Magnetic Bias. *Adv. Mater.* **2011**, *23*, 3853−3858.

(7) Russ, B.; Glaudell, A.; Urban, J. J.; Chabinyc, M. L.; Segalman, R. A. Organic thermoelectric materials for energy harvesting and temperature control. *Nature Reviews Materials* **2016**, *1*, 16050.

(8) Bubnova, O.; Khan, Z. U.; Malti, A.; Braun, S.; Fahlman, M.; Berggren, M.; Crispin, X. Optimization of the thermoelectric figure of merit in the conducting polymer poly(3,4-ethylenedioxythiophene). *Nat. Mater.* **2011**, *10*, 429−433.

(9) Mauritz, K. A.; Moore, R. B. State of Understanding of Nafion. *Chem. Rev.* **2004**, *104*, 4535−4586.

(10) Zhang, F. M.; Dong, L. Z.; Qin, J. S.; Guan, W.; Liu, J.; Li, S. L.; Lu, M.; Lan, Y. Q.; Su, Z. M.; Zhou, H. C. Effect of Imidazole Arrangements on Proton-Conductivity in Metal-Organic Frameworks. *J. Am. Chem. Soc.* **2017**, *139*, 6183−6189.

(11) Jamieson, F. C.; Domingo, E. B.; McCarthy-Ward, T.; Heeney, M.; Stingelin, N.; Durrant, J. R. Fullerene crystallisation as a key driver of charge separation in polymer/fullerene bulk heterojunction solar cells. *Chemical Science* **2012**, *3*, 485−492.

(12) Hiszpanski, A. M.; Baur, R. M.; Kim, B.; Tremblay, N. J.; Nuckolls, C.; Woll, A. R.; Loo, Y. L. Tuning polymorphism and orientation in organic semiconductor thin films via post-deposition processing. *J. Am. Chem. Soc.* **2014**, *136*, 15749−15756.

(13) Lan, S.; Yang, H.; Zhang, G.; Wu, X.; Chen, Q.; Chen, L.; Chen, H.; Guo, T. Importance of Solvent Removal Rate on the Morphology and Device Performance of Organic Photovoltaics with Solvent Annealing. *ACS Appl. Mater. Interfaces* **2017**, *9*, 20679−20685.

(14) Atkin, J. M.; Berweger, S.; Jones, A. C.; Raschke, M. B. Nano-optical imaging and spectroscopy of order, phases, and domains in complex solids. *Adv. Phys.* **2012**, *61*, 745−842.

(15) Mizoguchi, T.; Miyata, T.; Olovsson, W. Excitonic, vibrational, and van der Waals interactions in electron energy loss spectroscopy. *Ultramicroscopy* **2017**, *180*, 93−103.

(16) Teng, H. Overview of the Development of the Fluoropolymer Industry. *Appl. Sci.* **2012**, *2*, 496−512.

(17) Ebnesajjad, S. *Fluoroplastics*, Vol. *1*; William Andrew, 2014.

(18) Guenoun, G.; Faou, J.; Régnier, G.; Schmitt, N.; Roux, S. PTFE crystallization mechanisms: Insight from calorimetric and dilatometric experiments. *Polymer* **2020**, *193*, 122333.

(19) Bunn, C. W.; Cobbold, A. J.; Palmer, R. P. The fine structure of polytetrafluoroethylene. *J. Polym. Sci.* **1958**, *28*, 365−376.

(20) Bosq, N.; Guigo, N.; Zhuravlev, E.; Sbirrazzuoli, N. Nonisothermal crystallization of polytetrafluoroethylene in a wide range of cooling rates. *J. Phys. Chem. B* **2013**, *117*, 3407−3415.

(21) Eby, R. K.; Clark, E. S.; Farmer, B. L.; Piermarini, G. J.; Block, S. Crystal structure of poly(tetrafluoroethylene) homo- and copolymers in the high pressure phase. *Polymer* **1990**, *31*, 2227−2237.

(22) Clark, E. S. The Crystal Structure of Polytetrafluoroethylene, Forms I and IV. *J. Macromol. Sci., Part B: Phys.* **2006**, *45*, 201−213.

(23) Clark, E. S. The molecular conformations of polytetrafluoroethylene: forms II and IV. *Polymer* **1999**, *40*, 4659−4665.

(24) Weeks, J. J.; Clark, E. S.; Eby, R. K. Crystal structure of the low temperature phase (II) of polytetrafluoroethylene. *Polymer* **1981**, *22*, 1480−1486.

(25) Xu, X. G.; Rang, M.; Craig, I. M.; Raschke, M. B. Pushing the Sample-Size Limit of Infrared Vibrational Nanospectroscopy: From Monolayer toward Single Molecule Sensitivity. *J. Phys. Chem. Lett.* **2012**, *3*, 1836−1841.

(26) Atkin, J. M.; Sass, P. M.; Teichen, P. E.; Eaves, J. D.; Raschke, M. B. Nanoscale Probing of Dynamics in Local Molecular Environments. *J. Phys. Chem. Lett.* **2015**, *6*, 4616−4621.

(27) Panova, O.; Ophus, C.; Takacs, C. J.; Bustillo, K. C.; Balhorn, L.; Salleo, A.; Balsara, N.; Minor, A. M. Diffraction imaging of nanocrystalline structures in organic semiconductor molecular thin films. *Nat. Mater.* **2019**, *18*, 860−865.

(28) Ophus, C. Four-Dimensional Scanning Transmission Electron Microscopy (4D-STEM): From Scanning Nanodiffraction to Ptychography and Beyond. *Microsc. Microanal.* **2019**, *25*, 563−582.

(29) Quarti, C.; Milani, A.; Castiglioni, C. Ab Initio Calculation of the IR Spectrum of PTFE: Helical Symmetry and Defects. *J. Phys. Chem. B* **2013**, *117*, 706−718.

(30) Wilson, E. B. Some mathematical methods for the study of molecular vibrations. *J. Chem. Phys.* **1941**, *9*, 76−84.

(31) Cheatum, C. M.; Tokmakoff, A.; Knoester, J. Signatures of β-sheet secondary structures in linear and two-dimensional infrared spectroscopy. *J. Chem. Phys.* **2004**, *120*, 8201−8215.

(32) Song, X.; Chandler, D.; Marcus, R. A. Gaussian field model of dielectric solvation dynamics. *J. Phys. Chem.* **1996**, *100*, 11954−11959.

(33) Onsager, L. Electric Moments of Molecules in Liquids. *J. Am. Chem. Soc.* **1936**, *58*, 1486−1493.

(34) Thomas, H.; Brout, R. Molecular field theory, the onsager reaction field, and the spherical model. *J. Appl. Phys.* **1968**, *39*, 624−625.

(35) Masetti, G.; Cabassi, F.; Morelli, G.; Zerbi, G. Conformational Order and Disorder in Poly(tetrafluoroethylene) from the Infrared Spectrum. *Macromolecules* **1973**, *6*, 700−707.

(36) Weeks, J. J.; Eby, R. K.; Clark, E. S. Disorder in the crystal structures of phases I and II of copolymers of tetrafluoroethylene and hexafluoropropylene. *Polymer* **1981**, *22*, 1496−1499.

(37) Adisson, E.; Ribeiro, M.; Deffieux, A.; Fontanille, M. Evaluation of the heterogeneity in linear low-density polyethylene comonomer unit distribution by differential scanning calorimetry characterization of thermally treated samples. *Polymer* **1992**, *33*, 4337−4342.

(38) Pandey, A.; Champouret, Y.; Rastogi, S. Heterogeneity in the distribution of entanglement density during polymerization in disentangled ultrahigh molecular weight polyethylene. *Macromolecules* **2011**, *44*, 4952−4960.

(39) Rastogi, S.; Lippits, D. R.; Peters, G. W. M.; Graf, R.; Yao, Y.; Spiess, H. W. Heterogeneity in polymer melts from melting of polymer crystals. *Nat. Mater.* **2005**, *4*, 635−641.

(40) Zeng, Q. H.; Yu, A. B.; Lu, G. Q. Multiscale modeling and simulation of polymer nanocomposites. *Prog. Polym. Sci.* **2008**, *33*, 191−269.

(41) Aghadavoudi, F.; Golestanian, H.; Tadi Beni, Y. Investigating the effects of CNT aspect ratio and agglomeration on elastic constants of crosslinked polymer nanocomposite using multiscale modeling. *Polym. Compos.* **2018**, *39*, 4513−4523.

(42) Dong, K.; Liu, X.; Dong, H.; Zhang, X.; Zhang, S. Multiscale Studies on Ionic Liquids. *Chem. Rev.* **2017**, *117*, 6636−6695.

(43) Gooneie, A.; Schuschnigg, S.; Holzer, C. A Review of Multiscale Computational Methods in Polymeric Materials. *Polymers* **2017**, *9*, 16.

(44) Di Lorenzo, F.; Seiffert, S. Nanostructural heterogeneity in polymer networks and gels. *Polym. Chem.* **2015**, *6*, 5515−5528.

(45) Pollard, B.; Muller, E. A.; Hinrichs, K.; Raschke, M. B. Vibrational nano-spectroscopic imaging correlating structure with intermolecular coupling and dynamics. *Nat. Commun.* **2014**, *5*, 3587.

(46) Aoki, H.; Tanaka, S.; Ito, S.; Yamamoto, M. Nanometric Inhomogeneity of Polymer Network Investigated by Scanning Near-Field Optical Microscopy. *Macromolecules* **2000**, *33*, 9650−9656.

(47) Groves, C.; Reid, O. G.; Ginger, D. S. Heterogeneity in polymer solar cells: Local morphology and performance in organic photovoltaics studied with scanning probe microscopy. *Acc. Chem. Res.* **2010**, *43*, 612−620.